Volume 15, Issue 3, 152532 (1-12)

Iranian Journal of Catalysis (IJC)

https://doi.org/10.57647/j.ijc.2025.1503.32

Synthesis of $CuFe_2O_4$ nanoparticles for applications in biodiesel production and degradation of methylene blue dye

Narendra M. Patil[1], Nanasaheb P. Huse[2], Manohar R. Patil[1,*]

[1]*Nano-chemistry Research Lab, Department of Chemistry, Nandurbar Taluka Vidhayak Samiti's G. T. Patil Arts, Commerce and Science College, Nandurbar-425412, MH, India.*
[2]*Advanced Materials and Interface Lab, Department of Physics, Nandurbar Taluka Vidhayak Samiti's G. T. Patil Arts, Commerce and Science College, Nandurbar-425412, MH, India.*

[*]**Corresponding author:** profmanoharpatil@gmail.com

Original Research

Received:
17 February 2025
Revised:
1 April 2025
Accepted:
1 June 2025
Published online:
1 July 2025
Published in issue:
30 September 2025

Abstract:

Copper ferrite nanoparticles were synthesized using the traditional co-precipitation method. The estimated average crystallite size is approximately 42.30 nm, calculated using Scherer's formula. SEM images revealed an irregular and agglomerated morphology, suggesting a broad particle size distribution, which may influence the material's catalytic efficiency. The synthesized nanoparticles were successfully used for the degradation of the cationic dye Methylene Blue (MB), achieving a 94.2% removal efficiency from an aqueous solution at a concentration of 30 mg/L. In photocatalytic experiments, various parameters such as initial dye concentration, pH, and contact time were optimized to achieve efficient removal of MB dye. Furthermore, the copper ferrite nanoparticles were effectively utilized as a catalyst for the production of fatty acid methyl ester (FAME, or biodiesel) from oil extracted from algae. The algal oil was extracted using a Soxhlet apparatus. The optimum process conditions for maximum FAME yield (95.2%) were found to be: 10% (w/v) catalyst concentration, a 12:1 methanol-to-oil ratio, 180 minutes of reaction time, and a reaction temperature of 338 K. The biodiesel produced from algal oil and the free fatty acid composition of the algal oil were confirmed using GC and FT-IR techniques.

Keywords: Biodiesel; Copper ferrite nanoparticles; Methylene blue dye; SEM; XRD

1. Introduction

Water pollutants, such as dyes, have been an international problem. Color is the primary contaminant in wastewater. Dyes are utilized in exclusive industries, including paper, plastics, food, cosmetics, leather, pharmaceutical dyestuffs, textiles, etc., to color the product. As a result, an extensive quantity of coloration water is generated [1]. Even small portions of dyes can coloration large water bodies, which affects aesthetic benefits and reduces mild penetration wished for photosynthesis. Furthermore, many dyes are poisonous or carcinogenic [2]. Cationic dyes like Methylene blue have carcinogenic symptoms [3]. There are several approaches have been evolved for the elimination of artificial dyes from water and wastewater to lower their effect on the environment [4]. The dyes from the aqueous solution have been removed using methods like Adsorption, Advanced oxidation process, Photocatalytic degradation, Chemical precipitation, Sedimentation, flocculation, Phytoremediation, and bioremediation. Out of these adsorption process is a very renowned approach due the usage of low-price adsorbents and low-cost approach for water purification. The system of adsorption has an area over the opposite approach because of its sludge unfastened easy operation and eliminated dyes even from the diluted solution [5–9].

Copper ferrite ($CuFe_2O_4$) is a spinel-type ferrite with exceptional catalytic properties that make it a promising material for the degradation of dyes in wastewater treatment [10, 11]. Copper ferrite possesses a cubic spinel structure with unique electronic, magnetic, and surface characteristics. These properties contribute to its high catalytic activity.

Facilitates easy separation of the catalyst from the reaction medium using magnetic fields. Exhibits semiconducting behaviour, with a narrow bandgap (around $1.7 - 2.0$ eV), enabling efficient absorption of visible light. Highly resistant to degradation in various environmental conditions, making it reusable and sustainable. Copper ferrite is commonly employed as a photocatalyst, heterogeneous catalyst, or component in advanced oxidation processes (AOPs). The mechanisms include. Under visible light irradiation, $CuFe_2O_4$ generates electron-hole pairs [10]. These react with water and oxygen to produce reactive oxygen species (ROS) such as hydroxyl radicals ($^{\bullet}OH$) and superoxide anions ($O_2^{-\bullet}$), which break down dye molecules into less toxic substances. Copper ferrite can catalyze the decomposition of hydrogen peroxide (H_2O_2) into $^{\bullet}OH$ radicals, even under mild conditions, enhancing dye degradation. The combination of copper and iron in the spinel structure contributes to enhanced redox activity, boosting catalytic efficiency. Copper ferrite has been effectively used for the degradation of various synthetic dyes such as those commonly found in textile industries e.g., Methyl Orange [12], Congo Red [13, 14], E.g., Reactive Black 5 [15], E.g., Alizarin Red [16]. Besides this above application, nanoparticles have been used for biodiesel production from low-cost materials [17]. Energy is a basic requirement for human survival, so humans are searching for more energy-producing sources. The fuel is the basic source of energy, its natural reservoirs are limited, Hence, Researchers have studied more option for fuel production such as transesterification of waste cooking oil, Edible oil feed stock, Non edible oil feed stock such as neem seed oil has been performed using acid, bases, enzymes by homogeneous and heterogeneous catalysis methods [18–21]. We have done the application of copper ferrite nanoparticles in biodiesel production from Algae oil. Copper ferrite nanoparticles are used as heterogeneous catalyst for production of biodiesel from Algae oil. The application of copper ferrite nanoparticles in biodiesel production from algae is better due to their high catalytic efficiency, magnetic recoverability, reusability, and eco-friendliness. This novelty improves the economic viability and sustainability of biodiesel production, making it a promising alternative to traditional catalytic processes using NaOH and KOH.

Photocatalytic mechanism

The band gap (relative energy levels) of $CuFe_2O_4$ [conduction band (CB), valence band (VB)] is 1.85 eV as shown in Fig. 1 (a). Based on the results of the photocatalytic mechanism under UV-visible light irradiation proposed that the d orbital conducting band of $CuFe_2O_4$ has chemical bond interaction. According to the mechanism shown in the Fig. 1 (a), MB is adsorbed on the $CuFe_2O_4$ and was excited by UV-visible light irradiation. Subsequently, an electron is injected from the excited MB to the conducting band of $CuFe_2O_4$ where the electron is scavenged by molecular oxygen. The results are obtained with the $CuFe_2O_4$ as a catalyst under visible light irradiation, where the $CuFe_2O_4$ could serve to reduce the recombination of photo-generated electrons and holes by scavenging electrons. In this experiment, excited state electrons are readily injected into the d orbital (CB) of $CuFe_2O_4$ and subsequently transfer to the surface to react with water and oxygen which yield hydroxyl and superoxide radicals. This radical has oxidized the methylene blue (MB). The MB dye was finally converted to simple fragments of Carbon dioxide (CO_2) and Water (H_2O) [22–28].

2. Experimental

2.1 Materials and methods

Methylene Blue (MB) dye, $CuCl_2$ $2H_2O$, $FeCl_3{\cdot}6H_2O$ and Distilled water. All chemicals purchased from Merck India are limited to AR grade.

2.1.1 Synthesis method of copper ferrite nanoparticles using co-precipitation method

Dissolve copper chloride dihydrate and iron chloride hexahydrate in deionized water under constant stirring to prepare a homogeneous aqueous solution. To maintain a molar ratio of Cu^{2+} to Fe^{3+} as 1:2 (stoichiometric ratio of $CuFe_2O_4$). Heat the solution to 80 °C while stirring continuously. Add a precipitating agent (NH_4OH) dropwise

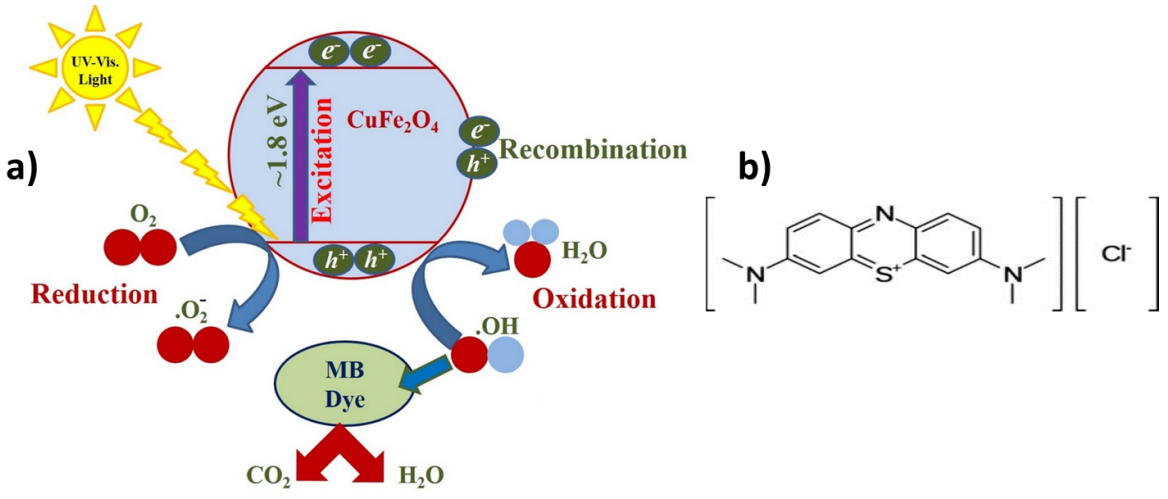

Figure 1. (a) Suggested photocatalytic degradation scheme for MB dye under UV-Vis. Light Irradiation in the presence of $CuFe_2O_4$. (b) Structure of Methylene Blue (MB dye).

to the metal ion solution under vigorous stirring. Maintain the pH around 11 to ensure complete precipitation of ferrite nanoparticles. A brownish precipitate of $CuFe_2O_4$ starts forming, indicating the formation of hydroxides. The precipitate is aged at an elevated temperature (80 °C) for 2 hours to promote uniform nanoparticle growth. The reaction mixture is stirred continuously to avoid agglomeration. The precipitate is separated using centrifugation at $\sim$ 5000 rpm for 10 minutes. It is washed multiple times with deionized water and ethanol to remove impurities. The pH is checked to ensure neutralization. The washed precipitate is dried in an oven at 80 °C for four hours to remove moisture [29, 30].

2.1.2 Photocatalytic degradation and absorbance measurement method

The water-soluble MB dye and $CuFe_2O_4$ is used as a photocatalyst. The photocatalytic degradation of MB dye was studied using a photocatalytic reactor and a mercury lamp with 260 Watts of power. A photocatalytic reactor equipped (Lelesil Innovations System) with a magnetic stirrer and chiller for water circulation and safety panel and double jacket quartz. All chemicals and reagents were of analytical grade purity. The stock solution is 1000 mg/lt of MB dye was prepared in double distilled water. In 50 mL of dye solution of the desired concentration, a different copper ferrite photocatalyst is added and stirred with a magnetic stirrer. At specific time intervals, a suitable aliquot of the sample is withdrawn and analyzed after centrifugation. A UV-visible double beam spectrophotometer (Systronics model-2203) at $\lambda_{max} = 664$ nm in our laboratory determines the changes in dye concentration.

$$\%\text{Degradation}(D) = \frac{C_0 - C_t}{C_t} \times 100 \tag{1}$$

The equation (1) is used to calculate the MB dyes photocatalytic degradation. C_0 is the initial concentration of MB dye and C_t is the concentration at time (t) for MB dye.

2.1.3 Soxhlet method for extraction of oil from Algae

The Algae were collected from stagnant water. The collected Algae biomass was dried in sunlight for 7 days. After complete drying, it was ground up to powder. The dried powder was fed in a round bottom flask of the Soxhlet apparatus (Model: Borosil Soxhlet 3840020). The hexane solvent was added in an appropriate amount in a round bottom flask. The content of the round bottom flask was heated at 80 °C for 8 hours. The oil was collected after every 20-minute cycle.

2.1.4 Biodiesel production

Requirements and chemicals: $CuFe_2O_4$ (Catalyst), Extracted oil from Algae and Methanol
Methods and experiment: Mixing of Copper ferrite as a heterogeneous catalyst and methanol was mixed with methanol and stirred properly for 20 min.
Biodiesel production: The mixture of catalyst and methanol was poured into oil extracted from Algae in a conical flask. The methanol and oil ratio taken for optimum condition is 12:1 (volumetric ratio). The following reaction and steps were followed.
Transesterification: The reaction process is called transesterification. The conical flask containing the solution was refluxed for 3 hours.
Settling: After shaking the solution was kept for 16 hours to settle the biodiesel and sediment layers.
Separation of FAME (biodiesel): The biodiesel was separated from sedimentation by flask separator carefully. Quantity sediment (glycerin, pigments, etc.) was measured.

3. Results and discussion

3.1 Structural properties

The copper ferrite nanomaterials were characterized by an X-ray Diffraction pattern (XRD), recorded on an X-ray Diffractometer, BRUKER (D8-Advance) with Cu Kα radiation ($\lambda = 1.5406$ Å) in the scanning range of $20 - 80°$ (2θ). All the diffraction peaks obtained in the XRD pattern are assigned to the reflection planes from the JCPDS card and are in good agreement with standard JCPDS data. Copper ferrite ($CuFe_2O_4$) crystallized in two different structures viz. tetragonal phase: associated with JCPDS Card #34-0425 and cubic phase: associated with JCPDS Card #25-0283. Fig. 2 (a) represents the XRD pattern (b) shows the Williamson-Hall (W-H) Plot and (c) represents the relationship between dislocation density and microstrain as a function of the crystallite size of Copper ferrite nanoparticles. The W-H method is used to analyze lattice strain from X-ray diffraction (XRD) data of copper ferrite. The positive slope of the fitted line suggests the presence of strain in the crystal lattice. The scattered data points suggest that the strain contribution may not be uniform across all crystallographic directions. Scattered data points indicate some deviation, likely due to instrumental broadening or sample imperfections [31]. The positive slope of the fitted line indicates the presence of microstrain in the material. As crystallite size increases, both dislocation density and microstrain decrease which is evident from Fig. 2 (c). This trend suggests that larger crystallite sizes correspond to lower structural defects and strain, which is common in well-crystallized materials [32, 33]. The sharp decrease in dislocation density at smaller crystallite sizes implies a high density of defects in nanoscale grains. The decreasing microstrain also indicates better lattice ordering and reduced internal stress with increasing crystallite size [33]. The estimated microstrain from W-H analysis was found to be 0.00274 which is nearly same as calculated from XRD analysis. The average crystallite size was estimated from the XRD data using Scherer's formula shown in Eq. (2) which was $\sim$ 42.30 nm for copper ferrite nanomaterials. The microstrain and dislocation density of copper ferrite nanomaterial samples were calculated from XRD data using the Eqs. (3) and (4) [34–36]

$$D(hkl) = \frac{0.9\lambda}{\beta \cos\theta} \tag{2}$$

$$\varepsilon = \frac{\beta \cos\theta}{4} \tag{3}$$

$$\delta = \frac{1}{D^2} \tag{4}$$

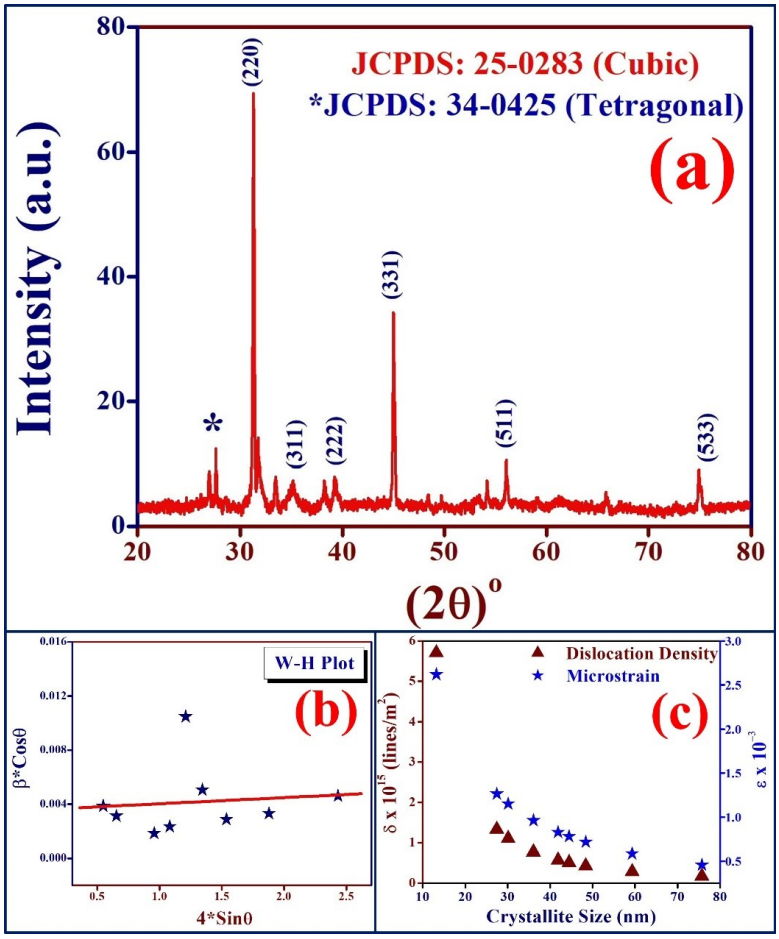

Figure 2. (a) Represents XRD pattern (b) Shows the Williamson-Hall Plot and (c) Shows dislocation density and microstrain vs. crystallite size of Copper ferrite nanoparticles.

The parameters like Dislocation Density (δ) (lines/m^2) and Microstrain (ε) (dimensionless), β is the full-width at half maximum (FWHM), D is the crystallite size, θ is the Bragg angle, ε is the microstrain are calculated and given in Table 1.

3.2 Morphological properties

The surface morphology and topography were examined by Field Emission Scanning Electron Microscopy (FE-SEM) HITACHI S-4800 as shown in Fig. 3. The scanning electron microscope (SEM) images showcase the morphology and surface characteristics of copper ferrite ($CuFe_2O_4$) at various resolutions, a material commonly used in biodiesel production and dye degradation applications due to its catalytic properties. The images reveal an irregular and agglomerated structure with particles of varying sizes with average size $\sim 100\ \mu$m. The presence of large and small granules suggests a broad particle size distribution, which may influence the material's catalytic efficiency. The rough surface texture indicates a high surface area, which is bene-

Table 1. The crystalline parameters estimated from copper ferrite XRD data.

(2θ)	β (rad)	$4*\sin\theta$	$\beta*\cos\theta$	D (nm)	$\delta \times 10^{14}$ (lines/m^2)	Microstrain
27.67	0.48313	0.956884	0.001831	75.72	1.74	0.000458
31.34	0.54721	1.080809	0.002337	59.33	2.84	0.000584
35.2	0.6146	1.209951	0.010475	13.23	57.07	0.002619
39.26	0.68549	1.344299	0.005053	27.43	13.28	0.001263
45.18	0.78886	1.537123	0.002864	48.4	4.27	0.000716
56.04	0.97848	1.879814	0.003309	41.9	5.69	0.000827
74.86	1.30708	2.432002	0.004602	30.12	11.02	0.001151
Average values				42.30	13.70	0.0011

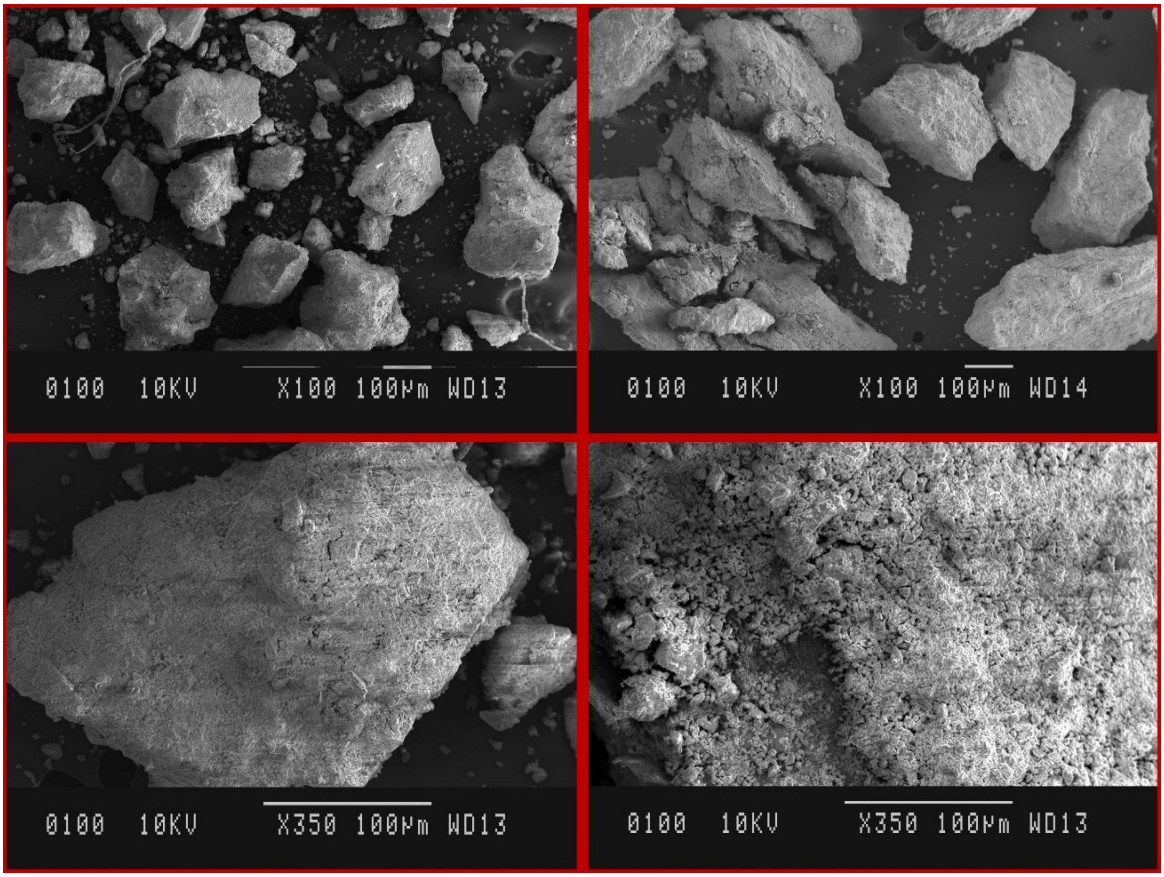

Figure 3. Shows the SEM images exhibiting the morphology of copper ferrite ($CuFe_2O_4$) at various resolutions.

ficial for catalytic applications, allowing more active sites for reactions [37]. The presence of micro- and nano-sized pores enhances mass transfer and improves the efficiency of dye degradation and transesterification reactions. The images display a well-defined crystalline structure with fractured and fragmented particles, which could be a result of synthesis conditions or post-processing treatments. Some fibrous or elongated structures are visible, potentially due to residual organic matter or synthesis byproducts. The rough, porous structure allows for efficient adsorption and interaction with oil molecules, enhancing the transesterification process. The increased surface area and active sites enable better adsorption and degradation of organic dyes in wastewater treatment applications. Overall, the SEM analysis confirms the suitability of copper ferrite as a catalyst, with its high surface area, rough morphology, and structural integrity, all contributing to its performance in biodiesel production and dye degradation [38]. Fig. 4 shows the SEM images marked with particles diameters and histogram representing the frequency distribution of particle diameters using ImageJ software to estimate the average particle size which was found to be $\sim 86\ \mu$m. The histogram

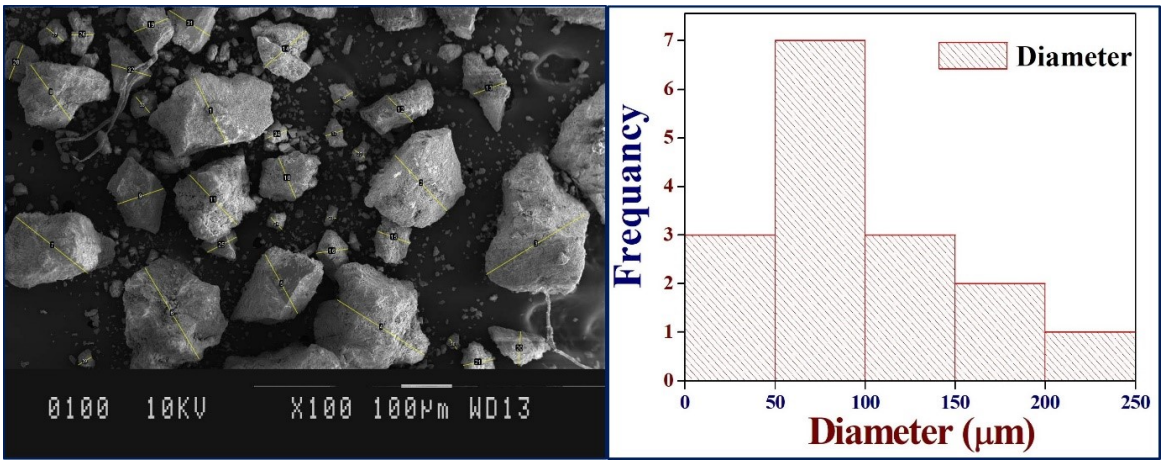

Figure 4. Shows the SEM images marked with particles diameter and histogram of average particle size distribution.

demonstrates that the majority of the particles fall within the $50-100\ \mu$m size range, followed by the $100-150\ \mu$m range. This distribution suggests that the particle population is skewed toward smaller sizes, with a few larger particles contributing to a tail at the upper end of the size spectrum.

3.3 Parametric study

The photocatalytic degradation of MB dye was studied at $\lambda_{max} = 664$ nm. The optimum condition for the removal of dyes is 30 mg/L, pH 9, and 0.2 gm Copper ferrite nanoparticles. The results obtained during this study are shown in Fig. 5- 7.

3.4 Effect of pH

A crucial parameter for the reaction occurring on the specific surface is pH, which is why the photocatalytic degradation of MB dye is investigated at various pH levels. The Systronics digital pH meter model is used for the experiment. In the pH range of $0-11$, at a dye concentration of 30 mg/L and a catalyst dose of 0.2 g, the role of pH in photocatalytic dye degradation is investigated. When the pH was raised to 9, it was found that the rate of photocatalytic degradation increased, as illustrated in Fig. 5. Dye surfaces become basic as pH rises. It binds to the $CuFe_2O_4$ in this basic form. As the pH rises, the dye molecules are repelled by the $CuFe_2O_4$ surface, which lowers the degradation efficiency of MB [39]. The pHZPC of copper ferrite is another reason to describe the adsorption followed by photocatalytic degradation of MB dye. The pHZPC of the copper ferrite is 7.5. This implies that when the pH of the dye solution is above pHZPC, the copper ferrite surface will be negatively charged, favoring cationic MB dye's adsorption. While below pHZPC, the copper ferrite surface becomes positively charged, and hence it favors the adsorption of MB dye due to electrostatic attraction. This adsorbed dye is degraded using a photocatalytic reactor [40].

3.5 Effect of initial dye concentration

The rate of degradation of MB dye is studied by varying the dye concentration from 10 to 100 mg/L because, for a fixed catalyst concentration, active sites remain the same. With the increase of the initial MB concentrations, the MB molecules accumulate on the surface of $CuFe_2O_4$. However, quenching between these excited MB molecules irradiated by UV-visible light will take place. The quenching probability could also increase with the increase of the initial MB concentrations. Consequently, the photocatalytic efficiency of the MB dye solution is decreased with the increase of the initial MB concentration, as shown in Fig. 6.

3.6 Effect of contact time

The effect of contact time for the photocatalytic degradation of MB dye by $CuFe_2O_4$ for varied MB dye concentrations ranges from 30 mg/L to 90 mg/L is shown in Fig. 7. By maintaining optimum conditions for MB dye degradation (as shown in Fig. 4 and 5) at concentration 30 mg/L, pH nine and a constant dose of copper ferrite 0.2 gm is added. The optimized dye solution is stirred with a magnetic stirrer. At specific time intervals, suitable sample aliquots are withdrawn and analyzed after centrifugation. A UV-Vis double-beam spectrophotometer (Systronics model 2203) at $\lambda_{max} = 664$ nm in our laboratory determines the changes in dye concentration.

The observation is that the MB dye is slowly degraded in the first 30 min, and then the degradation rate increases rapidly and reaches equilibrium in about 130 min. As the contact time increases further, there is repulsion between the dye molecules and the catalyst surface, leading to a decrease in photocatalytic efficiency. The rate of degradation of dye is initially slow because the surface of $CuFe_2O_4$ is not efficiently activated. As the surface gets activated, the rate of degradation of dye increases rapidly. Nearly 94.2% degradation of Methylene Blue dye occurred for 30 mg/L, pH 9, and a catalyst dose 0.2 gm.

3.7 Effect of catalyst dose

In this experiment, the effect of catalyst dose was studied in the range of 0.2 g/L to 2 g/L of optimized catalyst dose presented in Fig. 8. The 0.2 g/L catalyst dose was used as the optimum dose because higher doses of catalyst lead to a de-

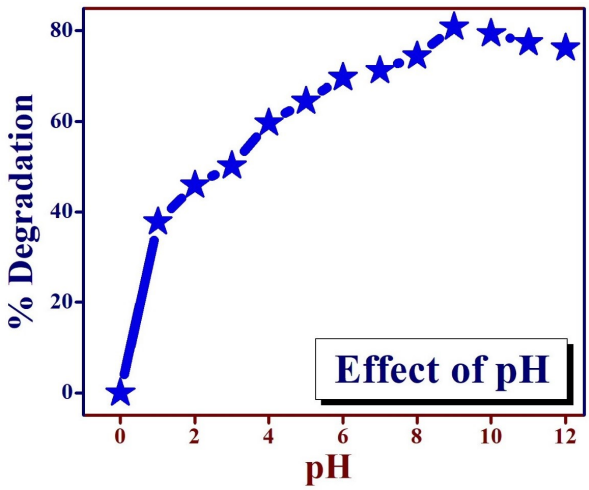

Figure 5. Effect of pH on the degradation of MB dye by $CuFe_2O_4$ at dye conc. 30 mg/L, catalyst dose 0.2 gm.

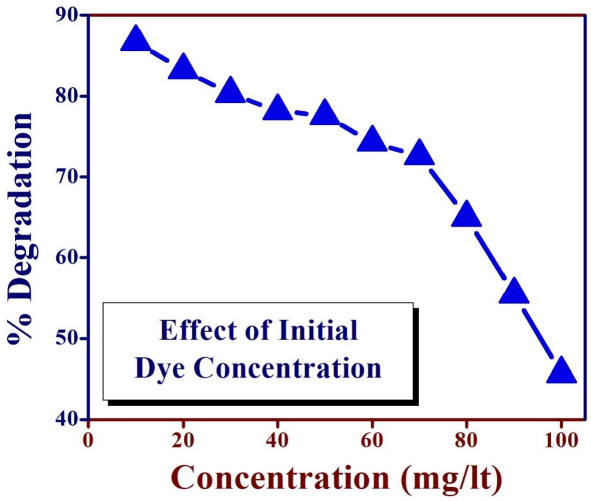

Figure 6. Effect of initial dye conc. on % degradation of MB dye by $CuFe_2O_4$ at pH 9.

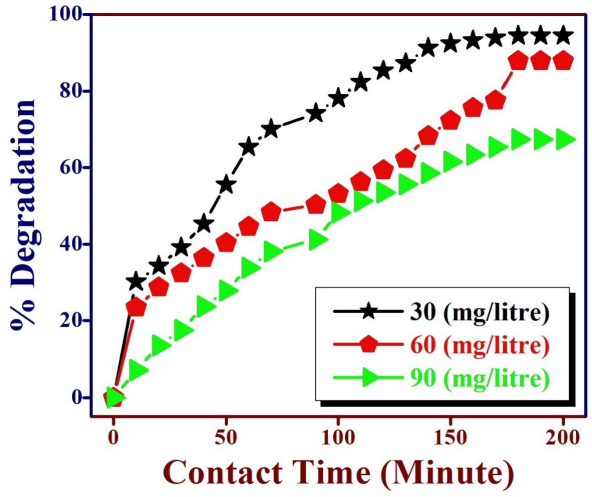

Figure 7. Effect of contact time on % degradation of MB dye and pH 9.

crease in the percent degradation of MB dye.his phenomena may be explained by the aggregation of nano-particles of the catalyst at dosage above 0.2 g/L causing a decrease in the number of surface active sites and increase in opacity and light scattering of the particles. Due to the aggregation of particles, some excited molecules of copper ferrite catalyst were deactivated by the ground state molecules of copper ferrite, which generates a lesser number of electron-hole pairs. It consequently decreases hydroxyl radical formation, which results in a decrease in the percent degradation of MB dye [41]. For 0.2 g/L, 94.2% degradation of MB dye, but for 2 g/L, only up to 67.4% was found, as shown in Fig. 8.

3.8 Recycling of copper ferrite nanoparticles

After conducting the MB dye degradation experiment we have done the following procedure for recycling copper ferrite Nanoparticles. The copper ferrite nanoparticles are centrifuged and well recovered with the help of the magnet. Then we washed it with deionized water and ethanol and dried it at 80 °C. We reused copper ferrite nanoparticles for biodiesel production.

4. $CuFe_2O_4$ for application in the production of Biodiesel from Algae

4.1 Mechanism for conversion of an Algae oil to Biodiesel

In the above reaction, oil (Specifically, the Authors have given an example of palmitic acid, which is one of the components of oil) reacts with methanol in the presence of copper ferrite as a heterogeneous catalyst. The free fatty acid groups are adsorbed on the acidic copper ferrite catalyst surface, promoting the esterification. Methanol acts as a nucleophile, which attacks the acidic site of the carbonyl group and forms an intermediate. Finally, the intermediate leads to the formation of the corresponding Fatty Acid Methyl Ester (FAME) as shown in the above Fig. 9.

4.2 Parametric Study for conversion of an Algae oil to Biodiesel

4.2.1 Catalyst dose

As the catalyst ($CuFe_2O_4$) dose increases conversion of extracted Algae oil into FAME (Biodiesel) also increases as shown in Fig. 10. Almost 95.2% conversion of Algal oil to Biodiesel is done at optimum conditions. The copper ferrite nanoparticles are magnetic and are easily separated and recovered [42].

4.2.2 Methanol to Oil ratio

As the Methanol to oil ratio increases conversion of extracted Algae oil into Biodiesel also decreases. Almost 95.2% conversion of Algal oil to Biodiesel is done at a Methanol: oil ratio of 12:1. The conversion of Algae oil to FAME (Biodiesel) at various Methanol: Oil ratios is shown in below Fig. 11.

4.2.3 Reaction temperature for transesterification

As the transesterification temperature increases, conversion of extracted Algae oil into FAME (Biodiesel) also increases. Almost 95.2% conversion of Algal oil to Biodiesel is done

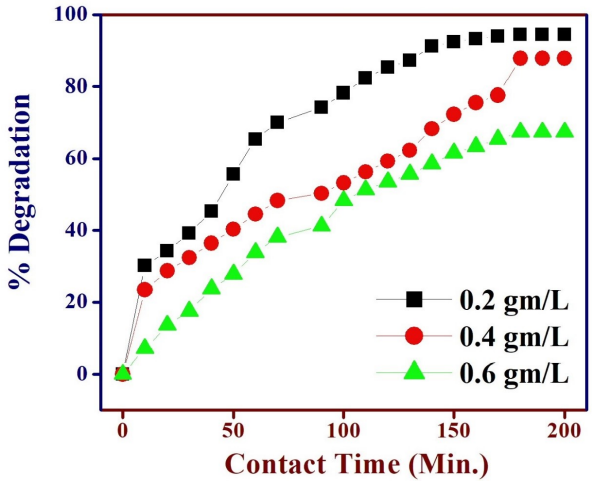

Figure 8. Effect of catalyst dose on % degradation of MB dye at pH ∼ 9 and 30 mg/L.

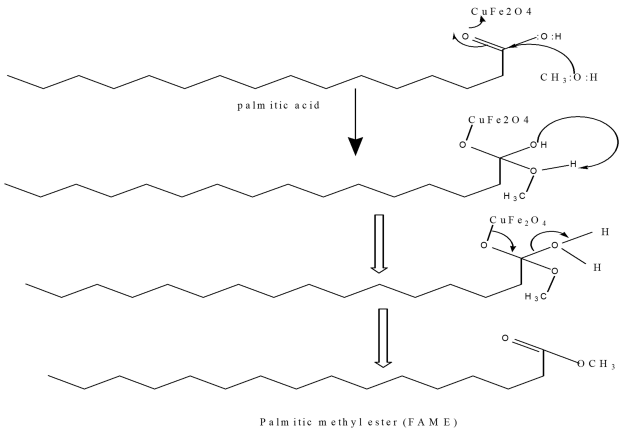

Figure 9. Proposed Reaction mechanism using copper ferrite as a heterogeneous catalyst for the conversion of palmitic acid to palmitic acid methyl ester.

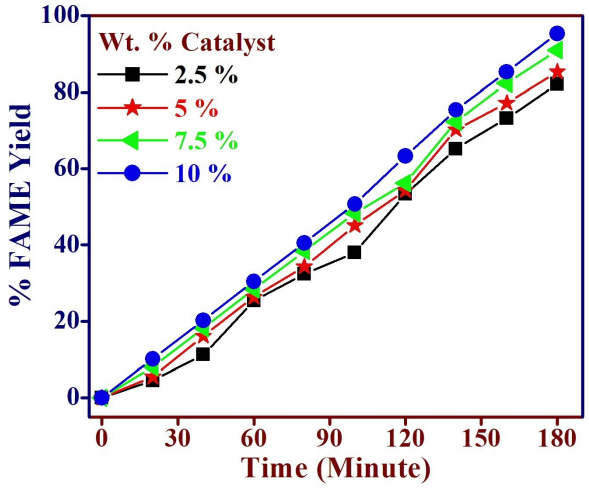

Figure 10. Effect of catalyst dose for conversion of Algae oil into FAME (Biodiesel).

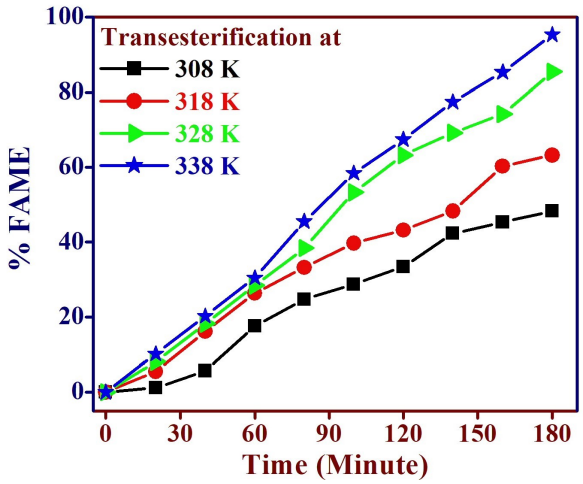

Figure 12. Effect of Reaction temperature for the transesterification of an Algae oil into FAME (Biodiesel).

at 338 K. The conversion of Algae oil to FAME (Biodiesel) at various reaction temperatures is shown in Fig. 12 below.

4.2.4 Characterization of Algal oil Biodiesel

The physicochemical properties of Algal oil Biodiesel were found according to the international standards specified in EN 14214 and ASTM D-6751. Viscosity and density match the requirements of EN 14214 and ASTM D-6751 standards. Since Biodiesel contains long hydrocarbon chains, its density is higher than that of petrochemical diesel. The viscosity of fuel could be effectively reduced by increasing the proportion of ethanol in the biodiesel mixture. Moreover, the diesel fuel in the engine plays a lubricating role, and the addition of algae oil Biodiesel to the fuel can effectively reduce the wear and corrosion of parts [43].

4.2.4.1. Viscosity

The commercial Biodiesel (ASTM Standard) has kinematic viscosity ranging from 1.9 to 6.0 mm^2/s at 40 °C and here prepared Biodiesel kinematic viscosity has been calculated by viscometer time flow method at 40°C is 2.8 mm^2/s. The prepared biodiesel viscosity is found closer to ASTM standard value as shown in Table 2.

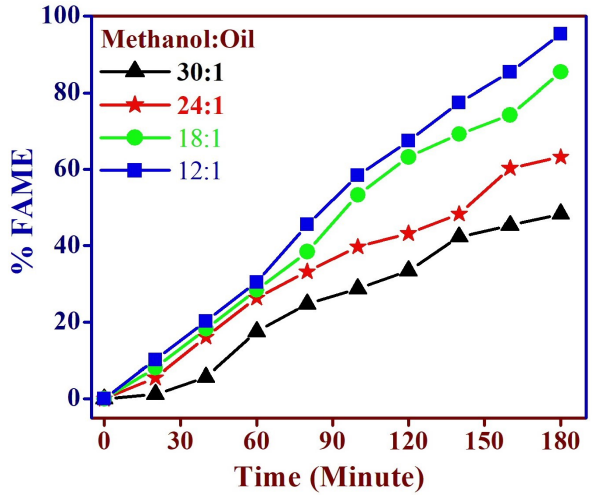

Figure 11. Effect of the oil ratio for the conversion of an Algae oil into FAME (Biodiesel).

4.2.4.2. Density

The commercial biodiesel (ASTM Standard) has a density of 0.87 g/cm^3 at 40 °C, and the prepared biodiesel density has been calculated by the specific gravity bottle method and is found to be 0.95 g/cm^3 at 40 °C. The prepared biodiesel density is found closer to the ASTM standard value as shown in Table 2.

4.2.4.3. Flash point

The flash point for biodiesel is 138 °C and according to ASTM Standards is 100 – 170 °C. The prepared biodiesel flash point is found closer to ASTM standard value as shown in Table 2.

4.2.4.4. FT-IR analysis of Algal oil and prepared Biodiesel

FT-IR analysis of algal oil and biodiesel shows almost identical peak positions, as shown in Fig. 13. The -CH- stretching frequency of the methyl group appeared within 2830 – 3005 cm^{-1}. The Carbonyl stretching frequency of oil containing an acid functional group occurred between 1730 – 1744 cm^{-1}. The carbonyl group (CO) stretching frequency of biodiesel containing an ester functional group occurred within 1744 – 1847 cm^{-1}. The slight variation peak is observed for C-O-R at 1027 cm^{-1}. This indicates the formation of the ester group in biodiesel.

4.2.4.5. Gas chromatography (GC) analysis of Algal oil and prepared Biodiesel

Fatty acid compositions of the sample were analyzed on a Shimadzu Gas chromatography GC-2014 model (Japan) using an FID detector as shown in Fig. 14. The injector and detector temperatures were set to 250 °C Nitrogen was used as carrier gas with a flow rate of 1 mL per min. The column used was DB-23 (Length 60 m, I.D. 0.25 mm, Film thickness ~ 0.20 μm, column max temp 250 °C, Make-Shimadzu). The oven method for the analysis was oven temperature 150 °C, hold for 3 min, raise temperature to 230 °C at a rate of 3 °C per min, hold for 3 min, again raise temperature to 250 °C, and hold for 5 minutes. Total method time was 42.33 min. The standards of the fatty

Table 2. Comparison of fuel properties of Algal oil Biodiesel with ASTM Standards.

Entry	Physical property	Calculated value	ASTM standard
1.	Viscosity	2.8 mm^2/s	1.9 to 6.0 mm^2/s
2.	Density	0.95 gm/cm^3	0.87 gm/cm^3
3.	Flash point	1380C	100 – 170 °C

acids were already injected on the same instrument using the same method.

The GC analysis of algal oil is conducted to determine the composition of free fatty acids in the corresponding oil. It shows the presence of Palmitic acid 9.26%, Stearic Acid 3.40%, Oleic acid 29.68%, Linoleic acid 55.23% as shown in Table 3.

The GC analysis of converted Algal oil to biodiesel (FAME) has been done. It shows the presence of Palmitic ester at retention time 11.243 with peak area 16.17%, Oleic ester at retention time 15.749 with peak area 27.65%, and Linolic ester at Retention time 17.14 with peak area 56.17%. This indicates sufficient conversion of fatty acid to fatty acid methyl ester using copper ferrite as the catalyst, as shown in Table 4.

5. Conclusion

In the present report, the Photocatalytic degradation of Methylene Blue (MB) dye is successfully carried out using copper ferrite nanoparticles. The XRD analysis of copper ferrite nanomaterials confirms their crystallization in both tetragonal and cubic phases, as verified by standard JCPDS data. The Williamson-Hall (W-H) analysis indicates the presence of microstrain within the crystal lattice, with non-uniform strain contributions across different crystallographic directions. A positive slope in the W-H plot confirms lattice strain, while the observed trend of decreasing dislocation density and microstrain with increasing crystallite size suggests improved lattice ordering and reduced structural defects. The estimated average crystallite size of $\sim$ 42.30 nm, calculated using Scherrer's formula, further supports the well-crystallized nature of the copper ferrite nanomaterials. The SEM analysis confirms the suitability of copper ferrite as a catalyst, with its high surface area, rough morphology, and structural integrity, all contributing to its performance in biodiesel production and dye degradation. Almost 94.2% of the MB dye is degraded after 180 minutes. After that catalyst, copper ferrite is recovered with the help of a magnet and utilized for the production of biodiesel. The biodiesel was successfully prepared from algae oil using copper ferrite nanoparticles as a catalyst. In previous research on biodiesel production, homogeneous catalysts like NaOH and KOH were used, but those are non-recoverable. In previous research, heterogeneous catalysts like CaO and MgO were also used, but those are non-magnetic and hence also non-recoverable. In the present report, we used heterogeneous catalysts like copper ferrite for biodiesel production, which is recovered and reusable. Also, we used Algae oil for the production of biodiesel. Algae is a naturally occurring biofeedstock

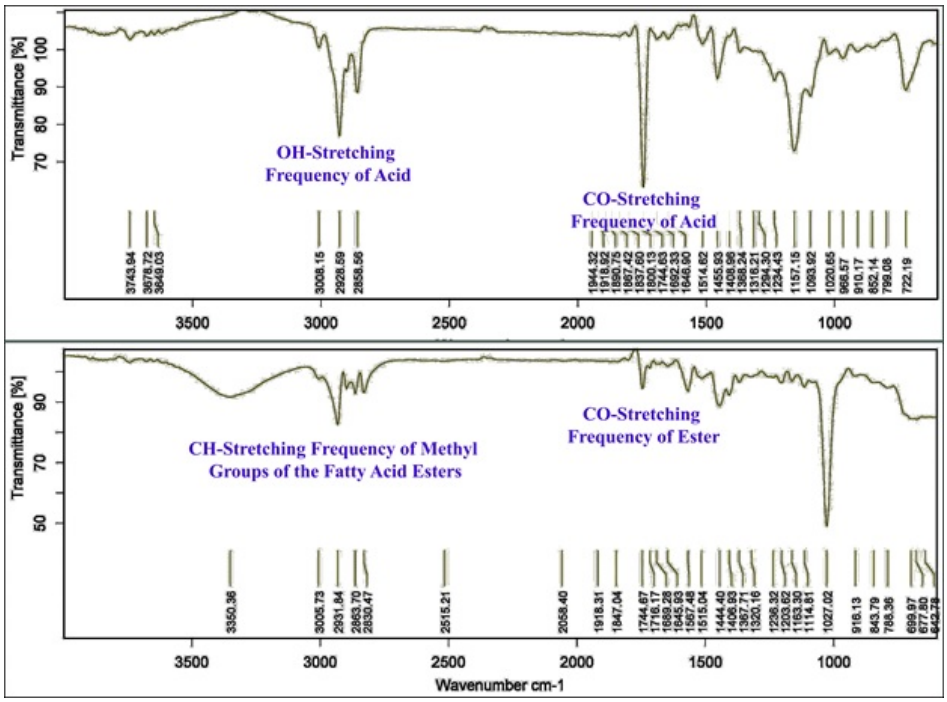

Figure 13. FT-IR analysis of an Algal oil and Biodiesel.

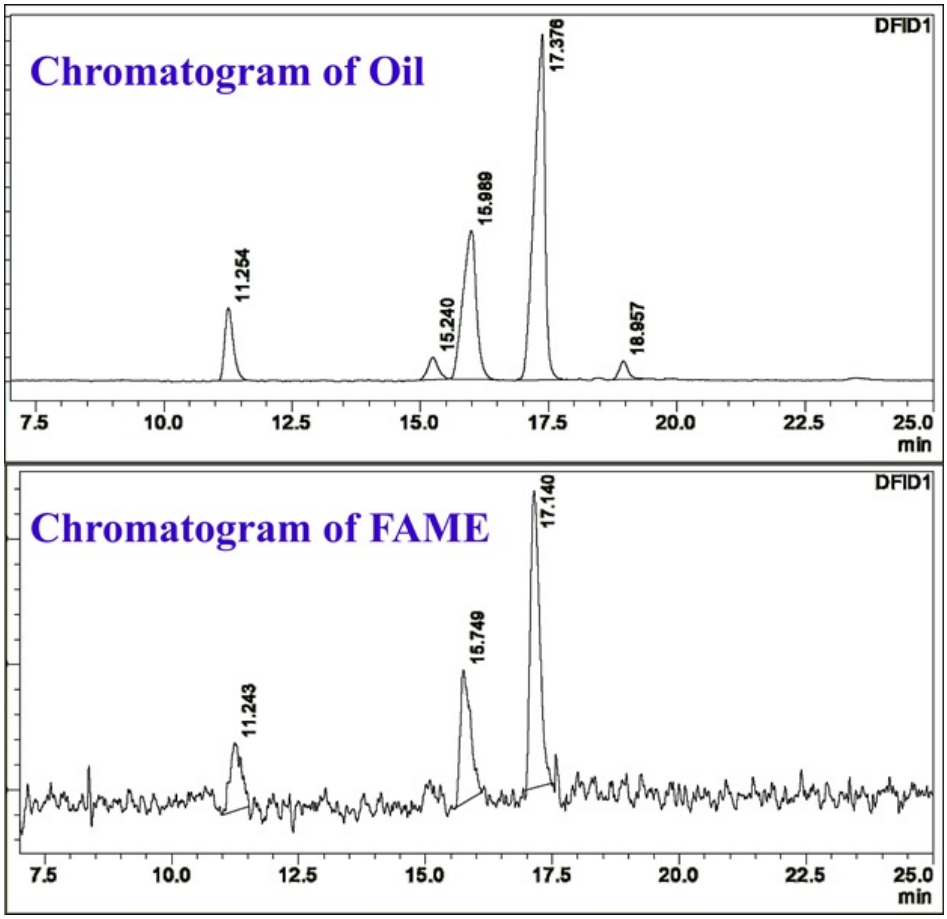

Figure 14. Gas chromatogram (GC) of Algae oil and product (FAME).

and hence is easily available in lakes, stagnant water, and rivers. So, overall, this report presents a cost-effective way for biodiesel production. As the catalyst dose increases, conversion of Algae oil into biodiesel also increases. The prepared biodiesel from algal oil and the free fatty acid composition of algal oil have been confirmed by GC and FT-IR techniques.

Acknowledgement

Authors are gratefully acknowledged by the SAIF, Punjab University Chandigarh for XRD and SEM studies. The authors are also thankful to the Principal of Nandurbar Taluka Vidhayak Samiti's, G. T. Patil Arts, Commerce and Science College, Nandurbar for providing necessary laboratory facilities.

Table 3. Showing the composition of Algal oil (free fatty acids).

Peak#	Name	Ret. Time	Area%	Area
1	Palmitic acid	11.254	9.263	701989
2	Stearic acid	15.24	3.404	257953
3	Oleic acid	15.989	29.689	2249861
4	Linoleic acid	17.376	55.233	4185615

Table 4. Showing the composition of prepared Biodiesel (FAME).

Peak#	Name	Ret. Time	Area%	Area
1	Palmitic ester	11.243	16.174	21518
2	Oleic ester	15.749	27.651	36788
3	Linoleic ester	17.14	56.175	74735

Authors contributions
Authors have contributed equally in preparing and writing the manuscript.

Availability of data and materials
The data that support the findings of this study are available from the corresponding author, upon reasonable request.

Conflict of interests
The author declare that they have no known competing financial interests or personal relationships that could have appeared to influence the work reported in this paper.

References

[1] R. Al-Tohamy, S. S. Ali, F. Li, K. M. Okasha, Y. A. G. Mahmoud, T. Elsamahy, H. Jiao, and Y. Fu. *J. Sun, Ecotoxic. Environ. Safety.*, **231**(2022):113160.
DOI: https://doi.org/10.1016/j.ecoenv.2021.113160.

[2] B. Carney Almroth, J. Cartine, C. Jönander, M. Karlsson, J. Langlois, M. Lindström, J. Lundin, N. Melander, A. Pesqueda, I. Rahmqvist, J. Renaux, J. Roos, F. Spilsbury, J. Svalin, H. Vestlund, L. Zhao, N. Asker, G. Ašmonaitė, L. Birgersson, T. Boloori, F. Book, and T. Lammel. *J. Sturve, Ecotoxic. Environ. Safety.*, **207**(2021):111523.
DOI: https://doi.org/10.1016/j.ecoenv.2020.111523.

[3] P. O. Oladoye, T. O. Ajiboye, E. O. Omotola, and O. J. Oyewola. *Results in Engin.*, **16**(2022):100678.
DOI: https://doi.org/10.1016/j.rineng.2022.100678.

[4] B. Lellis, C. Z. Fávaro-Polonio, J. A. Pamphile, and J. C. Polonio. *Biotech. Res. Innovation.*, **3**(2019):275–290.
DOI: https://doi.org/10.1016/j.biori.2019.09.001.

[5] A. Abbas, W. Sabbar, R. Abdul Salam, S. Faraj, and F. Abdulrazzak. *J. Mater. Environ. Sci.. 11 (2020) .*, **11**(2020):2007–2015.

[6] P. S. Kumar, G. J. Joshiba, C. C. Femina, P. Varshini, S. Priyadharshini, M. S. A. Karthick, and R. Jothirani. *Desalination and Water Treatment.*, **172**(2019):395–416.
DOI: https://doi.org/10.5004/dwt.2019.24613.

[7] M. T. Nguyen, M. D. Nguyen, T. H. Nguyen, M. Gao, N. Kaushik, O. V. Vasilyevich, A. A. Petrovna, O. N. Andreevich, N. K. Kaushik, T. T. Nguyen, and L. N. Nguyen. *Colloids and Surfaces A: Physicochemical and Engineering Aspects*, **705**(2025):135681.
DOI: https://doi.org/10.1016/j.colsurfa.2024.135681.

[8] M. R. Patil, S. D. Khairnar, and V. S. Shrivastava. *Appl. Nanosci.*, **6**(2016):495–502, .
DOI: https://doi.org/10.1007/s13204-015-0465-z.

[9] A. M. Aljeboree, A. N. Alshirifi, and A. F. Alkaim. *Arab. J. Chem.*, **10**(2017):S3381–S3393.
DOI: https://doi.org/10.1016/j.arabjc.2014.01.020.

[10] T. P. Oliveiraa nd S. F. Rodrigues, G. N. Marques, R. C. Viana Costa, C. G. Garçone Lopes, C. Aranas, A. Rojas, J. H. Gomes Rangel, and M. M. Oliveira. *Catalysts.*, **2**(2022):623.
DOI: https://doi.org/10.3390/catal12060623.

[11] H. Yang, J. Yan, Z. Lu, X. Cheng, and Y. Tang. *J. Alloy Comp.*, **476**(2009):715–719.
DOI: https://doi.org/10.1016/j.jallcom.2008.09.104.

[12] M. Vosoughifar. *J. Mater. Sci.: Mater. in Electronic.*, **27**(2016):10449–10453.
DOI: https://doi.org/10.1007/s10854-016-5133-x.

[13] V. S. Kirankumar, B. Hardik, and S. Sumathi. *IOP Conference Series: Materials Science and Engineering*, **263**(2017):022027.
DOI: https://doi.org/10.1088/1757-899X/263/2/022027.

[14] S. Sudarsan, M. Anandkumar, and E. A. Trofimov. *J. Indust. Engin. Chem.*, **131**(2024):208–220.
DOI: https://doi.org/10.1016/j.jiec.2023.10.020.

[15] K. Zaharieva, K. Milenova, V. Rives, R. Trujillano, Z. Zheleva, A. Eliyas, M. Tsvetkov, B. Kunev, and I. Mitov. *Bulgarian Chem. Commun.*, **47**(2015):105–111.

[16] Z. Khan, F. Ali, A. Said, U. Arif, K. Khan, N. Ali, G. Shabir, H. M. N. Iqbal, and M. Bilal. *Environmental Research*, **215**(2022):114148.
DOI: https://doi.org/10.1016/j.envres.2022.114148.

[17] H. C. Lima dos Santos, M. A. Gonçalves, A. da Cas Viegas, B. A. Miranda Figueira, P. T. Souza da Luz, G. Narciso da Rocha Filho, and L. R. Vieira da Conceição. *RSC Adv.*, **12**(2022):34614–34626.
DOI: https://doi.org/10.1039/D2RA06923G.

[18] D. T. Oyekunle, M. Barasa, E. A. Gendy, and S. K. Tiong. *Process Safety and Environmental Protection*, **177**(2023):844–867.
DOI: https://doi.org/10.1016/j.psep.2023.07.064.

[19] A. Iqbal, M. Imran, U.T. Wusqa, I. A. Alsafari, M. Tariq, M. Sirajuddin, F. A. Khan, M. N. Khan, and H. M. N. Iqbal. *Industrial Crops and Products*, **222**(2024):119801.
DOI: https://doi.org/10.1016/j.indcrop.2024.119801.

[20] M. Zeeshan, S. Ghazanfar, M. Tariq, H. M. Asif, A. Hussain, M. Usman, M. A. Khan, K. Mahmood, M. Sirajuddin, and M. Imran. *Renewable Energy*, **210**(2023):800–809.
DOI: https://doi.org/10.1016/j.renene.2023.04.077.

[21] R. Nayab, M. Imran, M. Ramzan, M. Tariq, M. B. Taj, M. N. Akhtar, and H. M. N. Iqbal. *Fuel.*, **328**(2022):125254.
DOI: https://doi.org/10.1016/j.fuel.2022.125254.

[22] A. Yousefi and A. Nezamzadeh-Ejhieh. *Iran. J. Catal.*, **11**(2024), .

[23] D. Patil, M. Sridhara, J. Manjanna, and S. Sabale. *Iran. J. Catal.*, **13**(2023):157–167, .
DOI: https://doi.org/10.30495/ijc.2023.1975703.1985.

[24] M. Rezaei, A. Nezamzadeh-Ejhieh, and A. R. Massah. *Ecotoxicology and Environmental Safety*, **269**(2024):115927.
DOI: https://doi.org/10.1016/j.ecoenv.2024.115927.

[25] S. A. Mirsalari, A. Nezamzadeh-Ejhieh, and A. R. Massah. *Spectrochimica Acta Part A: Molecular and Biomolecular Spectroscopy*, **288**(2023):122139.
DOI: https://doi.org/10.1016/j.saa.2022.122139.

[26] S. Ghattavi and A. Nezamzadeh-Ejhieh. *Composites Part B: Engineering.*, **183**(2020):107712.
DOI: https://doi.org/10.1016/j.compositesb.2019.107712.

[27] N. Mehrabanpour, A. Nezamzadeh-Ejhieh, S. Ghattavi, and A. Ershadi. *Applied Surface Science*, **614**(2023):156252.
DOI: https://doi.org/10.1016/j.apsusc.2022.156252.

[28] M. R. Alikhani, S. Saviz, and A. H. Sari. *Iran. J. Catal.*, **12**(2022):12007.
DOI: https://doi.org/10.30495/ijc.2022.691319.

[29] T. Dippong, E. A. Levei, and O. Cadar. *Nanomaterials*, **11**(2021):1560.
DOI: https://doi.org/10.3390/nano11061560.

[30] S. Patil and S. Jagadale. *ACS Omega.*, Chapter 3 - Co-precipitation methods for the synthesis of metal oxide nanostructures, In: Solution Methods for Metal Oxide Nanostructures. (2023):39–60.

[31] Q. Yousefi and A. Nezamzadeh-Ejhieh. *Solid State Sciences*, **154**(2024):107584, .
DOI: https://doi.org/10.1016/j.solidstatesciences.2024.107584.

[32] R. Sharma N.P. Huse, R.M. Patil. *ES Materials & Manufacturing*, **20**(2023):839.
DOI: https://doi.org/10.30919/esmm5f839.

[33] N. P. Huse, A. S. Dive, S. V. Mahajan, and R. Sharma. *J. Mater. Sci.: Materials in Electronics*, **29**(2018):5649–5658, .
DOI: https://doi.org/10.1007/s10854-018-8534-1.

[34] N. P. Huse, A. S. Dive, K. P. Gattu, and R. Sharma. *Materials Science in Semiconductor Processing.*, **67**(2017):62–68, .
DOI: https://doi.org/10.1016/j.mssp.2017.05.010.

[35] G. M. M. Gubari, S. M. Ibrahim Mohammed, N. P. Huse, A. S. Dive, and R. Sharma. *J. Electronic Mater.*, **47**(2018):6128–6135.
DOI: https://doi.org/10.1007/s11664-018-6491-3.

[36] N. Huse, D. Upadhye, and R. Sharma. *AIP Conference Proceedings*, **1728**(2016), .
DOI: https://doi.org/10.1063/1.4946461.

[37] J. Calvo de la Rosa and M. Segarra. *ACS Omega.*, **4**(2019):18289–18298.
DOI: https://doi.org/10.1021/acsomega.9b02295.

[38] M. M. El-Masry and R. Ramadan. *Applied Physics A.*, **128**(2022):110.
DOI: https://doi.org/10.1007/s00339-021-05238-6.

[39] V. Parimelazhagan, A. Chinta, G. G. Shetty, S. Maddasani, W.-L. Tseng, J. Ethiraj, G. Ayyakannu Sundaram, and A. S. K. Kumar. *Molecules*, **29**(2024):418.
DOI: https://doi.org/10.3390/molecules29020418.

[40] N. Omrani, A. Nezamzadeh-Ejhieh, and M. Alizadeh. *Desalination and Water Treatment*, **162**(2019):290–302.
DOI: https://doi.org/10.5004/dwt.2019.24352.

[41] A. Pourtaheri and A. Nezamzadeh-Ejhieh. *Chemical Engineering Research and Design*, **104**(2015):835–843.
DOI: https://doi.org/10.1016/j.cherd.2015.10.031.

[42] N. Masunga, O. K. Mmelesi, K. K. Kefeni, and B. B. Mamba. *J. Environment. Chem. Eng.*, **7**(2019):103179.
DOI: https://doi.org/10.1016/j.jece.2019.103179.

[43] Z. Li, S. Ding, C. Chen, S. Qu, L. Du, J. Lu, and J. Ding. *Energy Conversion and Management*, **192**(2019):335–345.
DOI: https://doi.org/10.1016/j.enconman.2019.04.053.